A micromechanical model for estimating the shear modulus and damping ratio of loose sands under low stresses

Application to a Mars regolith simulant

Caicedo, Bernardo; Chaparro, M. J.; Castillo Betancourt, J. P.; Cabrera, M. A.; Delage, P.; Lognonné, Ph; Banerdt, B.

DOI
10.1680/jgeot.23.00244

Publication date
2024

Document Version
Final published version

Published in
Geotechnique

A micromechanical model for estimating the shear modulus and damping ratio of loose sands under low stresses: application to a Mars regolith simulant

BERNARDO CAICEDO*, M. J. CHAPARRO*, J. P. CASTILLO BETANCOURT*†, M. A. CABRERA‡, P. DELAGE†, PH. LOGNONNÉ§ and B. BANERDT‖

The dynamic properties of loose sands under low stresses have been poorly investigated because of the higher order of magnitude of stress levels in terrestrial geotechnical structures. However, low densities and low stresses prevail in the sandy surface deposits of some other rocky planets, making low-stress conditions relevant for extra-terrestrial soil mechanics. This is the case for Mars, on the surface of which a seismometer has been placed during the InSight mission. In this context, a dynamic shear rheometer was used to measure the shear modulus and damping ratio of a Martian regolith simulant under very low stresses to improve the interpretation of the InSight dataset on surface materials. This paper also revisits the grain contact stiffness and the overall modulus of a random packing of identical spheres, based on the Hertz–Mindlin contact theory. A micromechanical model accounting for the effects of both grain roughness and slipping in the soil degradation curve is proposed. The results of the model show a good agreement with experimental data, capturing the non-linear transition from low to high shear strains. The model hence provides a new framework for a better understanding of the behaviour of granular materials in low-gravity (extra-terrestrial) conditions.

KEYWORDS: geotechnical engineering; granular materials; mathematical modelling; modulus of elasticity; seismic engineering

INTRODUCTION

The dynamic properties of loose sands under low stresses have been poorly investigated because of the higher order of magnitude of stress in most geotechnical structures on Earth. This is not the case at the surface of other (smaller) rocky planets, where low densities and low stresses prevail, like for the surface regolith at the InSight landing site on Mars. InSight (interior exploration using seismic investigations, geodesy and heat transport) is a geophysical mission managed by NASA with European space agencies (e.g. Centre National d'Etudes Spatiales (CNS), France and Deutschen Zentrum fuür Luft- und Raumfahrt (DLR), Germany) that successfully installed for the first time on the surface of Mars (in Elysium Planitia) a high-sensitivity very broad-band seismometer called SEIS (seismic experiment for interior structure), together with a self-driving thermal probe called HP^3 (heat flow and physical properties package) (Lognonné *et al*., 2019, 2020). Both instruments provided detailed geophysical and mechanical data of the near-surface terrain. Fig. 1 is a photograph taken at the beginning of the mission by the instrument context camera (ICC) of the InSight lander, showing that the landing site, called Homestead Hollow, is flat and characterised by a sandy deposit with little rock abundance, as planned from orbiter data during the landing site selection (Golombek *et al*., 2017). Fig. 1 also shows, in the centre, the semi-spherical white wind and thermal shield (WTS), covering the SEIS seismometer from Martian winds (under an average atmospheric pressure of 600 Pa) and temperature changes (between −20°C and −80°C).

Prior to the mission, the mechanical properties of some Mars regolith simulants were investigated in the laboratory (Delage *et al*., 2017). The selection of proper simulants was based on orbital thermal inertia measurements, geological considerations and some observations from former rover missions (Golombek *et al*., 2009, 2017, 2020), suggesting that the surface in Elysium Planitia is made up of loose sub-rounded to rounded sand with an average grain diameter of 175 μm. In this work, the regolith simulant used is the Fontainebleau sand (Andria-Ntoanina, 2011; Morgan *et al*., 2018; Mueller *et al*., 2021; Delage *et al*., 2022a). The shear modulus degradation and change in damping ratio under low stress and density similar to those expected on Mars are investigated by means of a new dynamic shear rheometer (Chaparro López *et al*., 2023). This apparatus works like a torsional cyclic shear apparatus but allows the shear modulus and damping ratio to be measured continuously along a broad range of shear strains ($10^{-7} < \gamma < 10^{-2}$, see Villacreses *et al*., (2020) and Chaparro López *et al*. (2023)). The experimental data obtained are used to propose a micromechanical model based on the Hertz–Mindlin approach, including the effect of the grain roughness and slipping (Hertz, 1882; Mindlin, 1949; Digby, 1981; Walton, 1987; Bachrach *et al*., 2000; Duffaut *et al*., 2010). The model also uses the Hashin–Shtrickman upper limit for calculating the transition from small to large strains (Hashin & Shtrikman, 1963). The results of the model show a good agreement with the experimental data, providing a framework for better understanding the evolution of shear modulus and damping ratio of granular materials with respect to the shear strain.

Manuscript received 2 August 2023; revised manuscript accepted 12 January 2024. First published online ahead of print 8 February 2024.
Discussion on this paper is welcomed by the editor.
* Universidad de los Andes, Bogota, Colombia.
† Ecole des Ponts ParisTech, Lab. Navier-CERMES, CNRS, UGE, Marne la Vallée, France.
‡ Faculty of Civil Engineering and Geosciences, Delft University of Technology, Delft, The Netherlands.
§ Université Paris-Cité, Institut de Physique du Globe, CNRS, Paris, France.
‖ Jet Propulsion Laboratory, California Institute of Technology, Pasadena, California, USA.

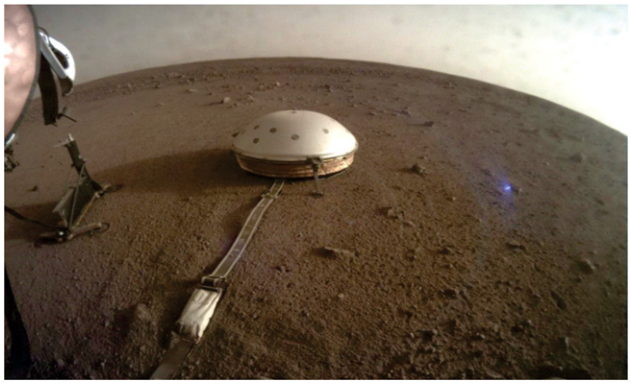

Fig. 1. Instrument context camera (ICC) photograph showing the white hemispherical wind and thermal shield (WTS) covering the SEIS seismometer and, on the left-hand side, the black support system of the self-penetrating dynamic thermal sensor of the HP^3 device. Image credit NASA – JPL

BACKGROUND

Since the 1970s, the dependency of the soil stiffness with respect to the strain amplitude has been recognised as a key factor in soil dynamics (Seed & Idriss, 1970; Hardin & Drnevich, 1972a). Under relatively small strains, the soil stiffness remains nearly constant, suggesting no significant changes between the inter-grain contact forces and hence no changes in the soil fabric (Reddy *et al.*, 2022). However, as strains grow, contact forces might shift and rearrange, leaving some grains free to move, initiating an accumulation of irreversible strains that is associated with decreased soil stiffness. This strain-dependent behaviour changes with grain size, relative density, degree of saturation and confinement pressure, among other things (Poblete *et al.*, 2015).

The soil degradation curve can be described through semi-empirical hyperbolic models, like that initially proposed by Hardin & Drnevich (1972b).

$$\frac{G}{G_0} = \frac{1}{1 + (\gamma/\gamma_r)} \tag{1}$$

where G is the secant shear modulus at any strain; G_0 is the elastic shear modulus (often measured at $\gamma \approx 10^{-6}$; and γ_r is a reference shear strain. More recently, Oztoprak & Bolton (2013) modified the hyperbolic model proposed by Darendeli (2001) with an extensive and detailed review of 454 tests, reporting the secant shear modulus degradation on a wide range of sands. Their model incorporates an elastic threshold strain γ_e and a curvature parameter a, as follows:

$$\frac{G}{G_0} = \frac{1}{1 + [(\gamma - \gamma_e)/\gamma_r]^a} \tag{2}$$

γ_e and a are fitting parameters, related to the effects of cementation and interlocking at small strains, that separate the instant when grain contacts start sliding. γ_r is an ad hoc reference strain, measured at $G/G_0 = 0{\cdot}5$. The simplicity of equation (2), its ease of use and the good fit with data resulted in its rapid adoption in the scientific community and in engineering practice (Hughes & Whittle, 2022). The efficiency of the model relies on the accuracy of G_0, which is found to be strongly influenced by the sand void ratio e, relative density D_R, uniformity coefficient C_u and mean effective stress p'. The database of Oztoprak & Bolton included tests in the low-stress range ($p' < 70$ kPa); however, the best fit was observed between 70 kPa and 600 kPa, leaving open the validity of the model for very low stresses ($p' = 70$ kPa). Finally, despite the low range in which γ_r, γ_e and a are found, the empirical nature hinders the generalisation of physically based interpretations. Here, this drawback is addressed by considering the grain contact stiffness and the stiffness of a random packing of identical spheres as an alternative to the existing models for soil stiffness degradation.

EXPERIMENTAL WORK

Material and methods

Various tests can be combined for measuring changes in soil stiffness at low and high strain. Low-strain tests (using the resonant column, the ultrasonic pulse or piezoelectric bender elements) allow the elastic response for $\gamma < 10^{-4}$ to be measured, while high-strain tests (using cyclic triaxial tests or cyclic simple shear tests) capture the soil degradation for $\gamma > 10^{-4}$ (e.g. Villacreses *et al.*, 2020). Although it is not guaranteed, combining low- and high-strain tests on the same material should yield a unique curve. Moreover, tests at low confining pressures are challenging and might hinder the material response, as the soil stiffness significantly decreases at lower strains. Therefore, Chaparro López *et al.* (2023) presented an alternative method by using a new dynamic shear rheometer (also known as the dynamic material analyser (DMA)) that allows a wide range of strains under low and high confining pressures to be covered. This work employs the DMA rheometer for studying the mechanical degradation of sand under low confining pressures and over a wide range of strains.

The DMA test is commonly used for determining the viscoelastic material properties of asphalt mixtures, such as the dynamic shear modulus and the phase angle at different temperatures. The technique is also recommended for evaluating the deterioration of asphalt materials and their performance with temperature control (Caro *et al.*, 2015). In the DMA test, a harmonic oscillatory angular strain with frequency and amplitude control is applied while measuring the stress necessary for maintaining the harmonic motion and the sample rotation with a torque precision of 10^{-9} Nm and an angular precision of 40 nrad (TA Instruments, 2007). The measuring principle of the DMA is similar to that of the cyclic torsional test currently used to characterise cyclic soil behaviour, but the DMA has better precision under very low strains (Chaparro López *et al.*, 2023).

The DMA test allows a direct and precise measurement of the dynamic shear modulus G and damping ratio. Usually, the DMA is used on viscoelastic materials without any confinement. In the present work, the authors adapted the specimen caps and used a latex membrane to apply, by vacuum through the bottom cap, a confining pressure to a dry sand sample (see Fig. 2). Consequently, the experimental procedure extends the capabilities of the DMA to fine-grained materials, allowing the investigation of the dynamic properties in a broader range of deformations and all in a single test.

Experiments are performed on Fontainebleau sand, which has a nearly monodisperse grain size distribution, mean grain diameter of 0·21 mm, uniformity coefficient $C_u = 1{\cdot}52$, void ratio range of $[e_{min} : e_{max}] = [0{\cdot}54 : 0{\cdot}94]$ and grain density of $\rho = 2{\cdot}65$ g/cm^3 (Andria-Ntoanina, 2011).

Loose sand samples ($e \approx e_{max}$) are often challenging to set up. To do so, DMA samples are prepared within a latex membrane and encapsulated within a rigid sliced pipe. The sliced pipe controls the sample dimensions, resulting in a sample of 15 mm dia. and 45 mm high. The available space between the rheometer pedestal and the piston restricts the sample height. Two O-rings tighten the latex membrane to the top and bottom DMA caps, ensuring a joined motion during testing (see Fig. 3).

The authors achieved loose sand samples with $D_R = 0{\cdot}26$ by a constant funnel discharge, ensuring no jamming within

the funnel and a filling height close to zero. Once the sample height has been reached and both caps are tight, the vacuum is applied on the bottom cap through a small orifice and the test is ready to start.

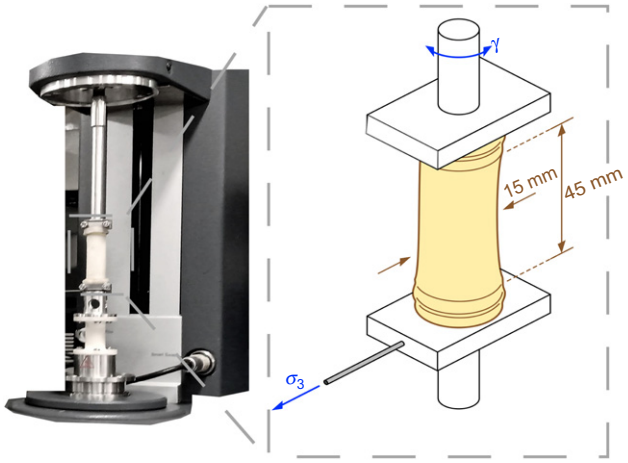

Fig. 2. Experimental set-up: sand sample in the dynamic shear rheometer (Chaparro López *et al.*, 2023)

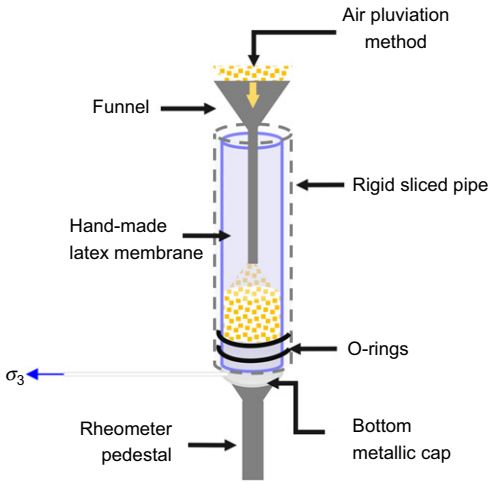

Fig. 3. Sample preparation (Chaparro López *et al.*, 2023)

The DMA test allows a sweep shear strain, ranging between $\gamma = [10^{-6} : 10^{-2}]$, maintaining a constant shear strain rate of 1 Hz over ten cycles. The modified DMA test allows the role of low confining pressure p' in sand samples to be studied using a 100 mbar suction pump, making it possible to investigate the transition between low and medium confining pressures, with $p' = [1, 3, 5, 7, 10, 20, 30]$ kPa. For $p' \leq 10$ kPa, a water-column manometer was used to control low confining pressures accurately. A full sweep shear strain was performed for each confining pressure, and three repetitions per confinement were carried out to check repeatability.

Experimental results

The recorded signals show a clean harmonic motion in time for both torque and rotation (see Fig. 4(a)). These signals are transformed into shear stress τ and shear strain γ, from which one derives the hysteretic loop. Then, as shown in Fig. 4(b), the secant shear modulus G is computed as the slope of the straight line joining the extremes of the hysteretic cycle.

The area of the hysteretic cycle represents the energy loss (ΔW) due to the accumulation of irreversible strains (Kramer, 1996). The damping ratio (ξ) is related to the ratio between ΔW and the maximum stored energy (W_s) as follows (Kramer, 1996):

$$\xi = \frac{1}{4\pi}\frac{\Delta W}{W_s} \tag{3}$$

The results in Fig. 5 show an increase in stiffness with increased confining pressure for $p' = [1, 10, 20, 30]$ kPa. For example, for $p' = 1$ kPa, the hysteresis loop has a slope close to zero because the sample is loose and the confining pressure low. The hysteresis loop inclination rises for $p' = 30$ kPa, indicating stiffening.

Figure 6 shows the changes in shear modulus G with respect to shear strain γ for different confining stress p'. Each test was repeated three times to assess the variability and the coefficient of variation (C_v) was computed for each confining pressure $p' = [1, 3, 5, 7, 10, 20, 30]$ kPa. The mean C_v across strain levels (γ) was $C_v = [22, 12, 11, 16, 30, 15, 26]\%$, showing good repeatability of the DMA test and an acceptable variability of the results. Moreover, the coefficient of variation remains in the

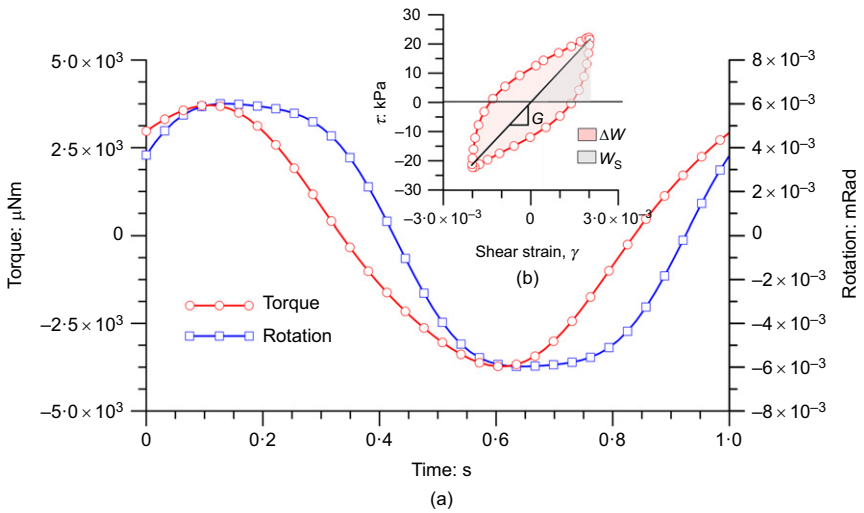

Fig. 4. Example of a single oscillation recorded in the DMA test. (a) Torque and displacement harmonic signal; (b) hysteretic loop indicating how the dynamic shear module G is determined as the loop slope; the red shaded area is related to the energy loss (ΔW) within the loop, and the grey shaded area is the maximum stored energy (W_s)

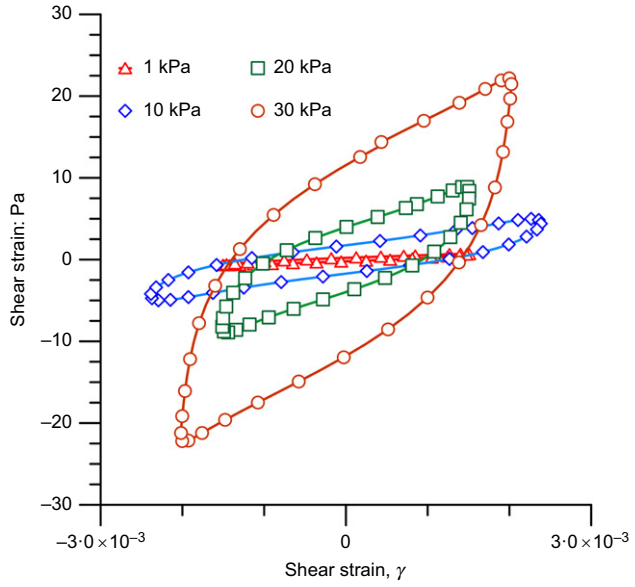

Fig. 5. Hysteretic loop showing the slope increase with increased confining pressure p' for $p' = [1, 10, 20, 30]$ kPa at 1 Hz

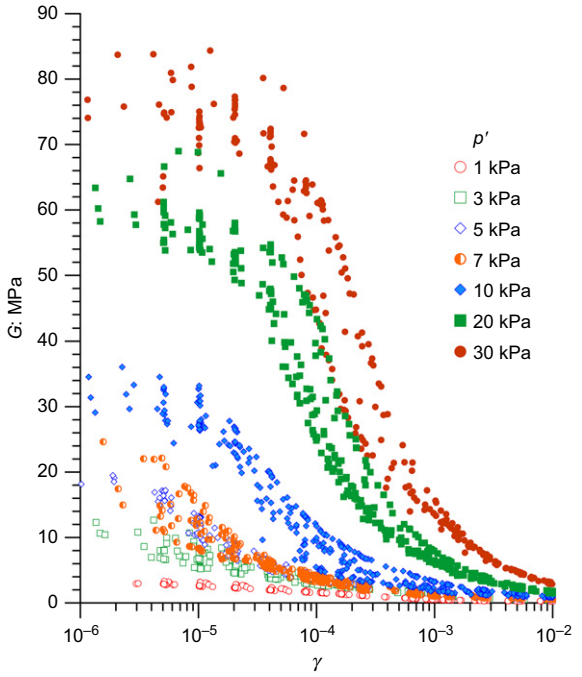

Fig. 6. Changes in shear modulus with respect to shear strain for different confining stress, $p' = [1, 3, 5, 7, 10, 20, 30]$ kPa at 1 Hz. Three tests were performed for each confining stress

same range for all strain levels. Indeed, for shear strain levels of $\gamma < 10^{-5}$, the C_v for the confining pressures $p' = [1, 3, 5, 7, 10, 20, 30]$ kPa, was $C_v = [18, 16, 11, 19, 29, 11, 19]\%$. Then, as the modulus degrades further and the shear strain increases to $10^{-4} < \gamma < 10^{-3}$, the C_v values are $C_v = [24, 9, 10, 15, 29, 18, 31]\%$. Finally, for higher strain levels ($\gamma > 10^{-3}$), when the shear modulus is completely degraded, the C_v is lower than 25% for all confining pressures – that is, $C_v = [23,7,15,4,25,10,10]\%$, showing a slight reduction in the dispersion of the results.

Figure 7 presents the differences in the changes in shear modulus G and damping ratio ξ with respect to the shear strain at low and high confining stresses (3 and 30 kPa, respectively). Fig. 7(a) shows that, under the low confining stress $p' = 3$ kPa, the material degradation starts under very low strains (10^{-6}). The degradation curve is close to linear, without observing any elastic range. In contrast, for $p' = 30$ kPa, the stiffness degradation starts at $\gamma \geq 10^{-5}$, and the shape of the degradation curve becomes sigmoidal. Fig. 7(b) shows that the change in damping ratio ξ is qualitatively in agreement with the degradation of the shear modulus G: for low confining stress p' (3 kPa), the damping ratio at low strains is high, with changes between 0·12 and 0·23, confirming the absence of any elastic range. Also, the shape of the curve is more regular and closer to linearity, like the degradation curve. Under 30 kPa, the damping ratio remains very low at small strains ($< 0{\cdot}01$ below 10^{-5}) prior to rapidly growing up to a maximum value of 0·30 for $\gamma > 10^{-5}$, in agreement with the degradation of the shear modulus shown in Fig. 7(a).

The experimental observations made with the data of Fig. 7 highlight the need for further investigation of the shear modulus degradation under low confining stresses and for rough grains, where both elastic and plastic behaviours are involved. A physically based formulation for this purpose is presented in the following section, based on an extension of the Hertz–Mindlin theory and accounting for the deformation of rough grains.

DERIVATION OF A NEW DEGRADATION MODEL BASED ON THE HERTZ–MINDLIN THEORY

Elastic properties of granular media based on the Hertz–Mindlin theory

The derivation of the expressions describing the elastic properties of granular media based on the Hertz theory is based on calculating the relative displacement of two spherical grains subjected to a normal contact force F_N, as shown in Fig. 8 (Hertz, 1882). The relative displacement between their centres $2\delta_H$ is

$$2(\delta_H)^{3/2} = 2\frac{3}{4}\frac{F_N}{E' R_g^{1/2}} \tag{4a}$$

$$\delta_H = \frac{a_H^2}{R_g} \tag{4b}$$

where E' is the effective modulus of elasticity given by $1/E' = (1\text{-}\nu_g^2)/E_g$; R_g is the grain radius. E_g and ν_g are the Young's modulus and Poisson's ratio of the grains, respectively, and a_H is the radius of the circular contact area, given by

$$a_H = \left(\frac{3F_N R_g}{4E'}\right)^{1/3} \tag{5}$$

Sub-index 'H' in variables a_H and δ_H denotes that they result from the Hertz theory.

In general, spheres i and j can have different radius R, different Young's modulus E and Poisson's ratio ν ($R_{i,j}$, $E_{i,j}$, $\nu_{i,j}$). In this case, the equivalent radius R_G^*, and the effective modulus of elasticity E' become:

$$\frac{1}{R_G^*} = \frac{1}{R_i} + \frac{1}{R_j} \tag{6}$$

$$\frac{1}{E'} = \frac{1-\nu_i^2}{E_i} + \frac{1-\nu_j^2}{E_j} \tag{7}$$

The Hertz–Mindlin (HM) theory (Hertz, 1882; Mindlin, 1949) allows the normal and shear stiffness of two elastic spheres, S_n^{HM} and S_t^{HM}, to be obtained, respectively (see

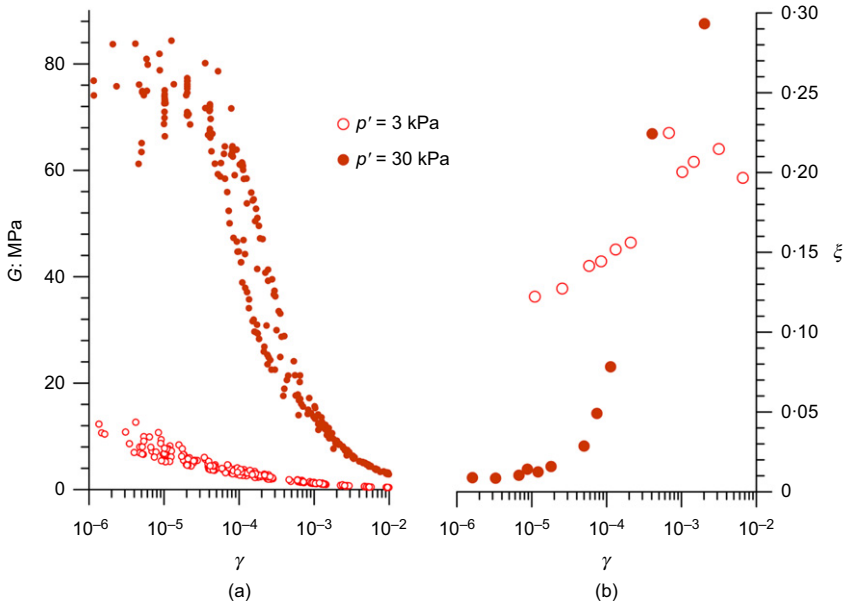

Fig. 7. Changes in (a) shear modulus G and (b) damping ratio ξ with respect to shear strain for low and high confining stress, p' = [3, 30] kPa at 1 Hz

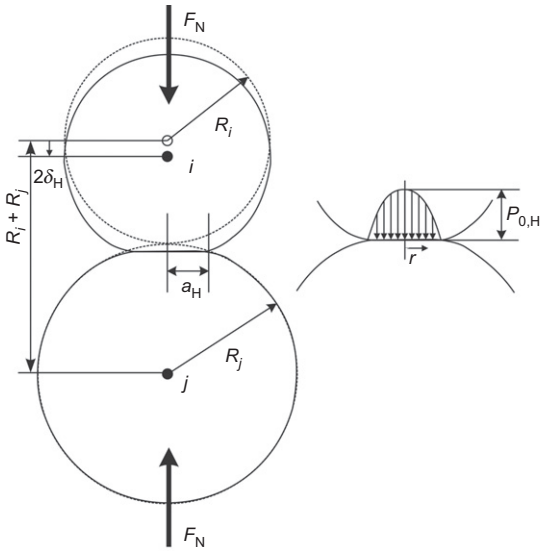

Fig. 8. Schematic drawing of two spherical grains subjected to a compressive load F_N, modified from Caicedo (2018)

Mavko *et al.*, 1998), as follows:

$$S_n^{HM} = \frac{4a_H G_g}{1 - \nu_g} \tag{8}$$

$$S_t^{HM} = \frac{8a_H G_g}{2 - \nu_g} \tag{9}$$

where G_g is the grain shear modulus.

Through statistical averaging, the Walton and Digby model (Digby, 1981; Walton, 1987) proposed the following expressions for the normal force F_N and the bulk (K_{HM}) and shear (G_{HM}) moduli of a pack of identical elastic spheres obeying the Hertz–Mindlin theory:

$$F_N = \frac{4\pi R_g^2 p'}{n(1-\phi)} \tag{10}$$

$$K_{HM} = \frac{n(1-\phi)}{12\pi R_g} S_n^{HM} \tag{11}$$

$$G_{HM} = \frac{n(1-\phi)}{20\pi R_g}\left(S_n^{HM} + 1{\cdot}5 S_t^{HM}\right) \tag{12}$$

where p' is the mean effective stress; n is the coordination number (average number of contacts per sphere); and ϕ is the porosity.

Finally, the contact stress $p(r)$ is assumed to be parabolically distributed on a circular contact by

$$p(r) = P_{0,H}\left[1 - \left(\frac{r}{a_H}\right)^2\right]^{1/2}, \text{ then } F_N = \frac{2}{3} P_{0,H} \pi a_H^2 \tag{13}$$

where $P_{0,H}$ is the maximum stress on the contact area.

Contact between rough spheres

The contact between rough particles has received much attention from both a geotechnical point of view (Yimsiri & Soga, 2000, 2011; Senetakis *et al.*, 2013a; Otsubo *et al.*, 2015; Altuhafi *et al.*, 2016; Nardelli & Coop, 2019) and a tribology one (Archard, 1957; Greenwood & Williamson, 1966; Greenwood & Tripp, 1967; Majumdar & Bhushan, 1991; Persson, 2006). Most researchers agree on the fact that, in rough contact surfaces, asperities decrease the contact stiffness. However, as the contact stress increases, asperities undergo plastic deformation and approach the relative displacement values given by Hertz (see Fig. 9).

Rigorous models for analysing the contact of rough spheres require an iterative solution of complex integral equations. Analytical models providing a closed-form system of equations are scarce. Among these, the model proposed by Bahrami *et al.* (2005) and modified by Butt *et al.* (2015) assumes that roughness is isotropic and randomly distributed (i.e. with a Gaussian distribution). The strength and size of asperities are described by their microhardness (H_{mic}) and root mean square (RMS) wave height (σ_{rms}), defined as the square root of the average of the squares of all wave heights, respectively. The Bahrami–Butt method uses

two non-dimensional parameters α_R and τ_R, as follows:

$$\alpha_R = \frac{\sigma_{rms} R_g}{a_H^2} \tag{14}$$

$$\tau_R = \frac{E'}{H_{mic}} \left(\frac{R_g}{\sigma_{rms}} \right)^{1/2} \tag{15}$$

By fitting the rigorous solution, Butt *et al.* (2015) proposed closed-form equations for computing three non-dimensional variables: the non-dimensional pressure distribution P'_0, the non-dimensional contact radius a'_R and the generalised pressure distribution exponent, γ_R, given by

$$P'_0 = \frac{1}{1 + 1{\cdot}22\alpha_R \tau_R^{-0{\cdot}16}} \tag{16}$$

$$a'_R = 1{\cdot}631P'_0 - 0{\cdot}496 - 0{\cdot}631P'_0 3{\cdot}358 \tag{17}$$

$$\gamma_R = 1{\cdot}5P'_0 a'_R 2 - 1 \tag{18}$$

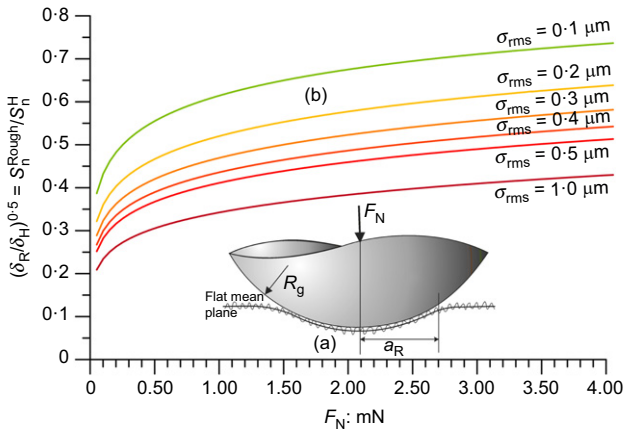

Fig. 9. (a) Schematic drawing of a smooth sphere resting on a deformable rough surface for the Bahrami–Butt model (Bahrami *et al.*, 2005; Butt *et al.*, 2015). (b) Effect of the size of asperities, σ_{rms}, and normal force F_N on the stiffness reduction ratio S_n^{Rough}/S_n^H. In the case of Fontainebleau sand, the curves are computed for grains with $R_g = 110$ μm, porosity $\phi = 0{\cdot}5$, coordination number $n = 6$ and asperities' microhardness $H_{mic} = 8{\cdot}2$ GPa as suggested in Yovanovich (2006) for quartz

These non-dimensional variables allow computing the radius of the rough contact area a_R, and the maximum contact stress P_0, as follows:

$$a_R = a'_R a_H \tag{19}$$

$$P_0 = (1 - \gamma_R) \frac{F_N}{\pi (a_R)^2} \tag{20}$$

Then, the maximum displacement at the centres of the contact area between rough grains, δ_R, is given by

$$\delta_R = \frac{P_0 a_R}{E'} f(\gamma_R) \tag{21}$$

where $f(\gamma_R)$ is a shape function formulated by Butt based on a beta function (further details are presented in the Appendix).

Equation (4b) indicates that the displacement between spheres is proportional to the square of the radius of the contact area between them ($\delta_H \propto a_H^2$). Likewise, equation (8) indicates that the radius of the contact area is proportional to the normal stiffness ($a_H \propto S_n^{HM}$). Therefore, the ratio between the stiffness of the rough surface grain and the ideal Hertzian stiffness of a smooth sphere S_n^{Rough}/S_n^{HM} becomes

$$\frac{S_n^{Rough}}{S_n^{HM}} = \left(\frac{\delta_R}{\delta_H} \right)^{1/2} \tag{22}$$

This ratio is obtained by calculating δ_H using equations (4b), (5) and (10), and by calculating δ_R using equation (21). This was done in Fig. 9, which shows that the reduction in contact stiffness is higher for lower stresses and decreases as the acting normal stress grows. In addition, the reduction ratio grows for larger asperities (i.e. high σ_{rms}).

Bachrach *et al.* (2000) consider the roughness of the particles by substituting in equation (5) the radius of the particles R_g with a contact radius R_c, which is much lower than the radius of the particles, $R_c = R_g$. This assumption modifies the Hertzian radius of the contact area a_H, which modifies the normal and shear stiffness. It is important to note that, considering equations (8) and (9), this assumption modifies the normal and shear contact stiffness in the same proportion. The same assumption is adopted in the present work. Therefore, the normal and shear stiffnesses S_n^{HM} and S_t^{HM} are affected by the same reduction ratio given in equation (22). Consequently, the bulk and shear moduli of a granular arrangement of identical rough spheres (K_R and G_R) become

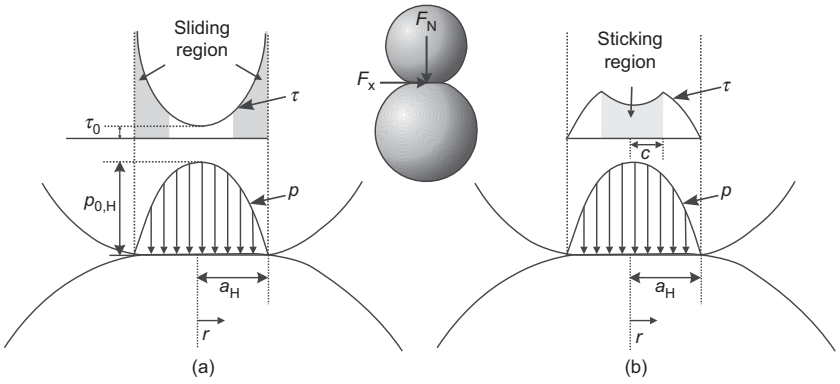

Fig. 10. (a) Contact normal and shear stresses given by the Hertz–Mindlin theory. (b) Sliding and sticking regions on the contact area, modified from Caicedo (2018)

$$K_{\mathrm{R}} = \frac{n(1-\phi)}{12\pi R_{\mathrm{g}}} S_{\mathrm{n}}^{\mathrm{HM}} \left(\frac{\delta_{\mathrm{R}}}{\delta_{\mathrm{H}}}\right)^{1/2} \tag{23}$$

$$G_{\mathrm{R}} = \frac{n(1-\phi)}{20\pi R_{\mathrm{g}}} \left(S_{\mathrm{n}}^{\mathrm{HM}} + 1{\cdot}5 S_{\mathrm{t}}^{\mathrm{HM}}\right) \left(\frac{\delta_{\mathrm{R}}}{\delta_{\mathrm{H}}}\right)^{1/2} \tag{24}$$

Friction-dependent shear modulus

In a larger collection of grains, even under hydrostatic stress, the shear and compressive forces (F_x and F_{N}, respectively) act simultaneously and as a function of the grain assembly (Radjai *et al.*, 1996). In such a condition, as shown in Fig. 10, the shear stress $\tau(r)$ on a point located at a radius r of the contact area results from a tangential load F_x, given by the Mindlin solution as

$$\tau(r) = \tau_0 \left[1 - \left(\frac{r}{a_{\mathrm{H}}}\right)^2\right]^{-1/2}$$
$$F_x = 2\tau_0 \pi a_{\mathrm{H}}^2 \tag{25}$$

where τ_0 is the shear stress at the middle of the contact area and r is the radius in the contact area.

Equation (25) leads to infinite shear stress at the contact area perimeter (see Fig. 10(a)). Moreover, the normal stress decreases near the contact area perimeter. In contrast, the shear stress increases until it exceeds Coulomb's friction law. Therefore, a more realistic approach consists in dividing the contact area into two regions (see Fig. 10(b)): (*a*) a sliding region in which the shear contact stress is $\tau = \mu p$ (where μ is the friction coefficient and p is the normal contact stress) and (*b*) a circular sticking region of radius c. The relationship between these radii is given by the following equation (Popov, 2010):

$$\frac{c}{a_{\mathrm{H}}} = \left(1 - \frac{F_x}{\mu F_{\mathrm{N}}}\right)^{1/3} \tag{26}$$

To obtain the shear modulus accounting for the effect of sliding grains, G_{RS}, Duffaut *et al.* (2010) suggest affecting the shear stiffness of equation (24) by the ratio c/a_{H} given by equation (26). However, to link inter-grain contact forces with stresses, it is possible to change $F_x/\mu F_{\mathrm{N}}$ in equation (26) by the normalised mobilised shear strength τ_{mob}, as follows:

$$G_{\mathrm{RS}} = \frac{n(1-\phi)}{20\pi R_{\mathrm{g}}} \left[S_{\mathrm{n}}^{\mathrm{HM}} + 1{\cdot}5 S_{\mathrm{t}}^{\mathrm{HM}} (1-\tau_{\mathrm{mob}})^{1/3}\right] \left(\frac{\delta_{\mathrm{R}}}{\delta_{\mathrm{H}}}\right)^{1/2},$$
$$\tau_{\mathrm{mob}} = \frac{\tau}{\mu p'} \tag{27}$$

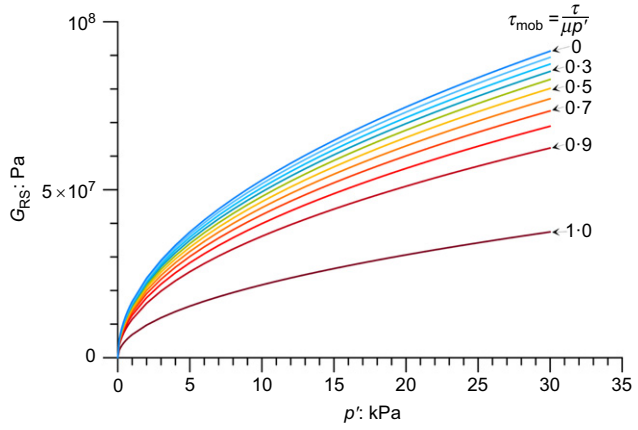

Fig. 11. Effect of the normalised mobilised shear stress on the shear modulus. Results are computed for grains with $R_{\mathrm{g}} = 110$ μm, porosity $\phi = 0{\cdot}5$, coordination number $n = 6$, asperities $\sigma_{\mathrm{rms}} = 0{\cdot}8$ mm and microhardness $H_{\mathrm{mic}} = 8{\cdot}2$ GPa

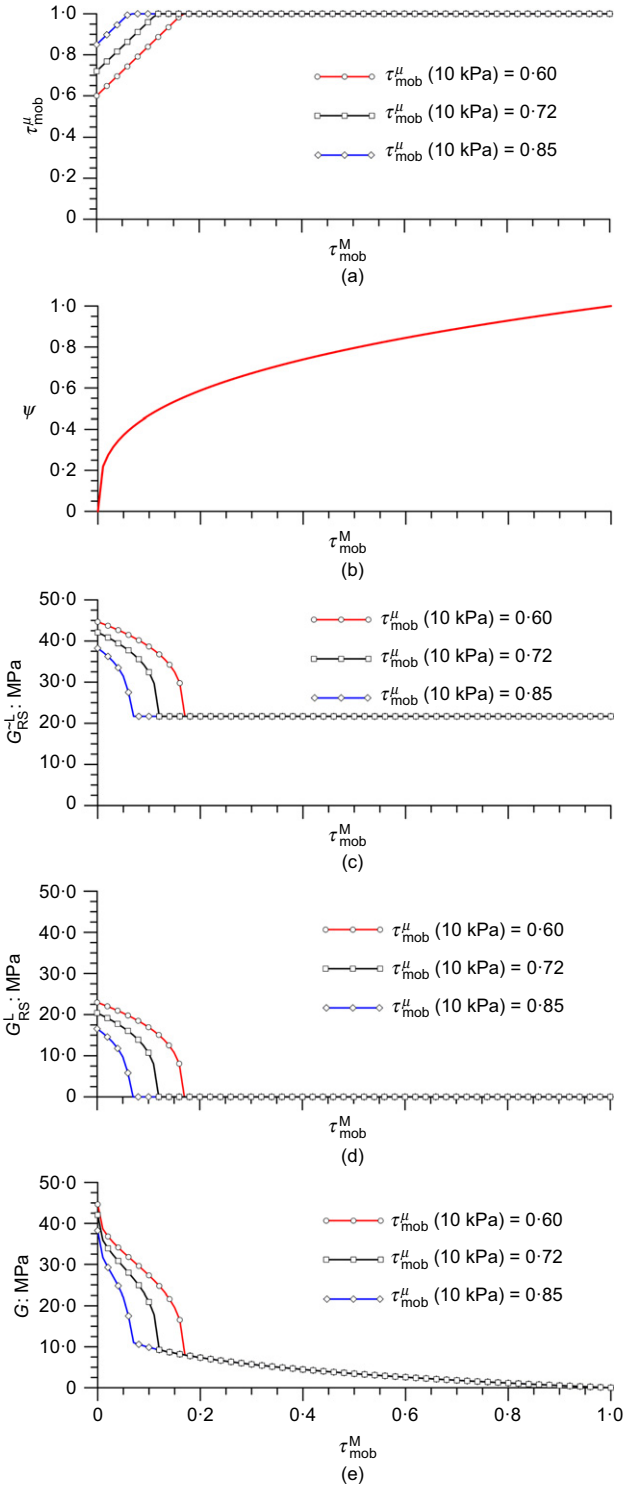

Fig. 12. Details of the procedure for computing the degradation of the shear modulus: (a) evolution of $\tau^{\mu}_{\mathrm{mob}}$ with respect to $\tau^{\mathrm{M}}_{\mathrm{mob}}$; (b) proportion ψ of material without shear strain localisation with respect to $\tau^{\mathrm{M}}_{\mathrm{mob}}$; (c) shear modulus of material without localisation $G^{-\mathrm{L}}_{\mathrm{RS}}$; (d) shear modulus of material with localization $G^{\mathrm{L}}_{\mathrm{RS}}$; (e) shear modulus of the mixture $G(\tau^{\mathrm{M}}_{\mathrm{mob}})$

Figure 11 shows the effect of the mobilised shear strength on the shear modulus G_{RS} calculated using equation (27). As expected, G_{RS} decreases as the mobilised shear stress increases. However, one observes that, even for a total mobilisation of the shear strength, the shear modulus does not decrease to zero. This is due to the contribution of the normal stiffness S_n^{HM} into the shear modulus, given by equation (27). However, this contribution is expected to vanish when there is localisation of shear strains in the soil.

Transition from small to large strains

Using the previous theoretical framework for simulating the transition from small to large strains requires the adoption of the following hypotheses.

(*a*) H1. At the inter-grain level, shear strength is mobilised even when subjected to isotropic confining stress. This hypothesis agrees with the Mindlin solution, demonstrating that shear stress increases to infinite even when the grains undergo very small tangential loads. This hypothesis also agrees with Bachrach *et al.* (2000), Duffaut *et al.* (2010) and Castillo Betancourt *et al.* (2023), who demonstrated that experimental measurements of the Poisson's ratio of dry granular materials subjected to hydrostatic stresses can only be explained theoretically by assuming the existence of a given proportion of sliding grains.

(*b*) H2. The normalised shear strength mobilisation occurs at two scales – namely, at the grain scale and at the element scale – herein microscopic and macroscopic, τ_{mob}^{μ} and τ_{mob}^{M}, respectively.

(*c*) H3. τ_{mob}^{μ} and τ_{mob}^{M} increases at the same rate up to $\tau_{mob}^{\mu} = 1$, a value at which the shear stiffness becomes null.

(*d*) H4. For a given τ_{mob}^{M}, there is a volumetric portion of grains ψ whose shear modulus is given by equation (28) and a complementary portion $(1 - \psi)$ for which there is no effect of the normal stiffness S_n^{HM} on the shear modulus (see equation (29)). These distinct behaviours result from the localisation of shear strains. Moreover, the combined shear modulus from these behaviours can be calculated using the Hashin–Shtrikman upper-bound formulation shown in equation (30) (Hashin & Shtrikman, 1963).

(*e*) H5. Following equation (26), it is assumed that the portion of grains ψ depends on the macroscopic normalised shear strength to a power of 1/3 – that is, $\psi = (\tau_{mob}^{M})^{1/3}$. This assumption does not have any theoretical support, but it is justified by the good agreement with the experimental results shown in the next section 'Performance of the micromechanical model for the whole range of confining stresses'.

(*f*) H6. Normalised shear strength mobilisation does not affect the soil bulk modulus.

The previous hypotheses suggest the following procedure for calculating the shear modulus corresponding to a given macroscopic shear strain mobilisation $G(\tau_{mob}^{M})$. Fig. 12 illustrates the methodology applied for a confining stress of 10 kPa.

(*a*) First, according to hypothesis H1, it is necessary to assume the inter-grain shear strength mobilisation for the confining stress p', denoted as $\tau_{mob}^{\mu}(p')$. This variable can be obtained fitting the shear modulus experimental measurements at very low strains ($\gamma < 10^{-5}$). Three values of $\tau_{mob}^{\mu}(p')$ are assumed in Fig. 12(a), $\tau_{mob}^{\mu}(p') = [0{\cdot}60; 0{\cdot}72; 0{\cdot}85]$.

(*b*) Second, for a given macroscopic normalised shear strength mobilisation τ_{mob}^{M}, hypothesis H3 indicates that the microscopic normalised shear strength mobilisation is $\tau_{mob}^{\mu} = \tau_{mob}^{M} + \tau_{mob}^{\mu}(p') \leq 1$. Fig. 12(a) illustrates the evolution of $\tau_{mob}^{\mu}(p')$ for the three initial assumed values.

(*c*) According to hypothesis H5, the proportion of grains affected by the localisation of shear strength is $\psi = (\tau_{mob}^{M})^{1/3}$. The evolution of proportion ψ is shown in Fig. 12(b).

(*d*) From hypotheses H4 and H6, the shear and bulk moduli of the two distinct portions of grains are as follows.

Portion of grains without localisation (see Fig. 12(c)):

$$G_{RS}^{\not\sim L}(\tau_{mob}^{M}) = \frac{n(1-\phi)}{20\pi R_g}\left[S_n^{HM} + 1{\cdot}5S_t^{HM}\left(1-\tau_{mob}^{\mu}\right)^{1/3}\right] \times \left(\frac{\delta_R}{\delta_H}\right)^{1/2} \tag{28}$$

Portion of grains with localisation (see Fig. 12(d)):

$$G_{RS}^{L}(\tau_{mob}^{M}) = \frac{n(1-\phi)}{20\pi R_g}\left[1{\cdot}5S_t^{HM}\left(1-\tau_{mob}^{\mu}\right)^{1/3}\right] \times \left(\frac{\delta_R}{\delta_H}\right)^{1/2} \tag{29}$$

(*e*) Using the Hashin–Shtrikman upper bound, as shown in Fig. 12(e), the combined shear modulus become

$$G(\tau_{mob}^{M}) = G_{RS}^{\not\sim L} + \frac{1-\psi}{\left(G_{RS}^{L} - G_{RS}^{\not\sim L}\right)^{-1} + \left[2\psi\left(K_R + 2G_{RS}^{\not\sim L}\right)\right] / \left\{5G_{RS}^{\not\sim L}\left[K_R + (4/3)G_{RS}^{\not\sim L}\right]\right\}} \tag{30}$$

(*f*) Finally, the macroscopic shear strain corresponding to a given τ_{mob}^{M} is computed as the ratio between the macroscopic shear stress τ and the shear modulus $G(\tau_{mob}^{M})$. As a result, the macroscopic shear stress is given by the product of the macroscopic friction coefficient, μ^{M}, the confining stress p' and the macroscopic shear strength mobilisation (i.e. $\tau = \mu^{M} p' \tau_{mob}{}^{M}$). Therefore, the macroscopic shear strain become

$$\gamma(\tau_{mob}^{M}) = \frac{\tau}{G(\tau_{mob}^{M})} = \frac{\mu^{M} p' \tau_{mob}^{M}}{G(\tau_{mob}^{M})} \tag{31}$$

(*g*) It is usual to relate the decrement in shear modulus to the growth of the damping ratio. Equation (32) gives an empirical equation that allows the damping ratio to be computed for a particular macroscopic normalised shear strength mobilisation, $\xi(\tau_{mob}^{M})$. However, in the case of very loose sands, according to hypothesis H1, there is

some shear strength mobilisation even for low strains, so the damping ratio begins with a non-zero value given by $\xi^{\mu}\tau_{\mathrm{mob}}{}^{\mu}(p')$, where ξ^{μ} is a model parameter. Then, as the mobilisation of the shear strength increases, the shear modulus $G(\tau^{\mathrm{M}}_{\mathrm{mob}})$ decreases and the damping ratio increases. An exponent of 3 is used in equation (32) to account for the increase in damping ratio. This exponent is the inverse of the exponent used in the relationship proposed in hypothesis H5. Then, ξ^{M} is another model parameter computed a

$$\xi\left(\tau^{\mathrm{M}}_{\mathrm{mob}}\right) = \xi^{\mu}\tau^{\mu}_{\mathrm{mob}}(p') + \left[\xi^{\mathrm{M}} - \xi^{\mu}\tau^{\mu}_{\mathrm{mob}}(p')\right] \times \left[\frac{G_0 - G\left(\tau^{\mathrm{M}}_{\mathrm{mob}}\right)}{G_0}\right]^3 \quad (32)$$

Finally, after computing the shear modulus $G(\tau^{\mathrm{M}}_{\mathrm{mob}})$, it is possible to compute the shear strain γ using equation (31). It is also possible to compute the damping ratio using equation (32). Fig. 13 shows a comparison between the experimental results obtained for $p' = 10$ kPa, demonstrating very good agreement. The performance of the model is further discussed in the following section.

PERFORMANCE OF THE MICROMECHANICAL MODEL FOR THE WHOLE RANGE OF CONFINING STRESSES

The proposed model uses several physical parameters that relate properties at the scale of the grains (i.e. R_{g}, G_{g}, v_{g}, σ_{rms}, H_{mic}, μ) and at the scale of a collection of grains (i.e. ϕ, n, μ^{M}). Table 1 summarises these values, indicating whether they were directly measured on Fontainebleau sand or adopted from previous works on similar silica sands. In addition, as

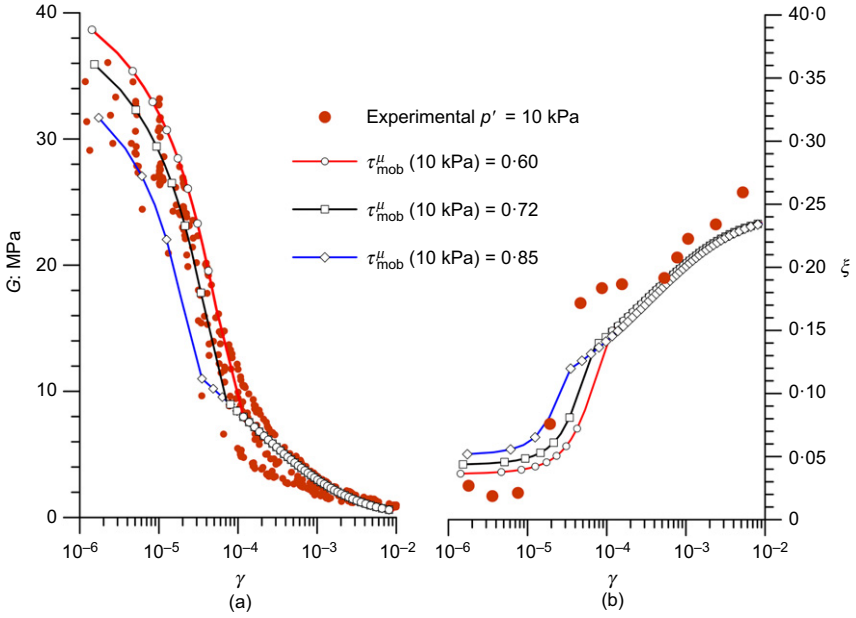

Fig. 13. Comparison between the experimental results and the theoretical model for $p' = 10$ kPa for three values of $\tau^{\mu}_{\mathrm{mob}}(p') = [060; 0{\cdot}72; 0{\cdot}85]$: (a) shear modulus degradation curve; (b) damping ratio. The parameters of the theoretical model are given in Table 1

Table 1. Parameters of the micromechanical model

Parameter		Comment	References
Porosity	$\phi = 0{\cdot}455$	Sample porosity measured in tests	Delage *et al.* (2022a, 2022b)
Coordination number	$n = 6$	Value for a loose arrangement of uniform spheres.	Mavko *et al.* (1998), Caicedo (2018)
Grain size	$R_{\mathrm{g}} = 110$ μm	Assuming $R_{\mathrm{g}} = D_{50}/2$, knowing that the Fontainebleau sand has a well-sorted grain size distribution with a $D_{50} = 220$ μm.	Castillo Betancourt *et al.* (2023)
Grain's shear modulus	$G_{\mathrm{g}} = 44$ GPa	For silica grains	Bachrach *et al.* (2000)
Grain's Poisson's ratio	$v_{\mathrm{g}} = 0{\cdot}08$	For silica sands	Bachrach *et al.* (2000)
Microhardness of the asperities	$H_{\mathrm{mic}} = 8$ GPa	For silica sands	Yovanovich (2006)
Asperities' height	$\sigma_{\mathrm{rms}} = 0{\cdot}7$ μm	Based on the fitting of Poisson's ratio in Caicedo *et al.* (2023)	Caicedo *et al.* (2023)
Inter-grain shear strength mobilisation	$\tau^{\mu}_{\mathrm{mob}}(p')$	Fitted curve given in equation (33)	No reference
Micro friction coefficient	$\mu = 0{\cdot}23$	Based on the measurements of Leighton Buzzard sand	Senetakis *et al.* (2013a, 2023b)
Macroscopic friction coefficient	$\mu^{\mathrm{M}} = 0{\cdot}55$	Corresponding to a friction angle of 29° for loose Fontainebleau sand	Andria-Ntoanina (2011)
Damping ratio coefficient	$\xi^{\mu} = 0{\cdot}03$	Fitting parameter	No reference
Damping ratio coefficient	ξ^{M}	Fitted curve given by equation (34)	No reference

stated in hypothesis H1, it is necessary to adopt an initial microscopic normalised shear strength mobilisation value $\tau^{\mu}_{\mathrm{mob}}(p')$ to reproduce the change in shape of the shear modulus degradation curve. The experimental results suggest that $\tau^{\mu}_{\mathrm{mob}}(p')$ is high for low confining stresses and decreases when the confining stress grows. The following sigmoidal equation was obtained from the experimental results.

$$\tau^{\mu}_{\mathrm{mob}}(p') = 1 - \frac{1}{1 + \mathrm{e}^{-0{\cdot}28(p'-13{\cdot}8)}} \quad (p' \text{ in kPa}) \tag{33}$$

Fitting the damping ratio curves is more empirical; it requires two parameters, ξ^{μ} and ξ^{M}. Parameter ξ^{μ} controls the damping ratio at low strains and can be taken as constant ($\xi^{\mu} = 0{\cdot}06$). However, parameter ξ^{M}, which controls the

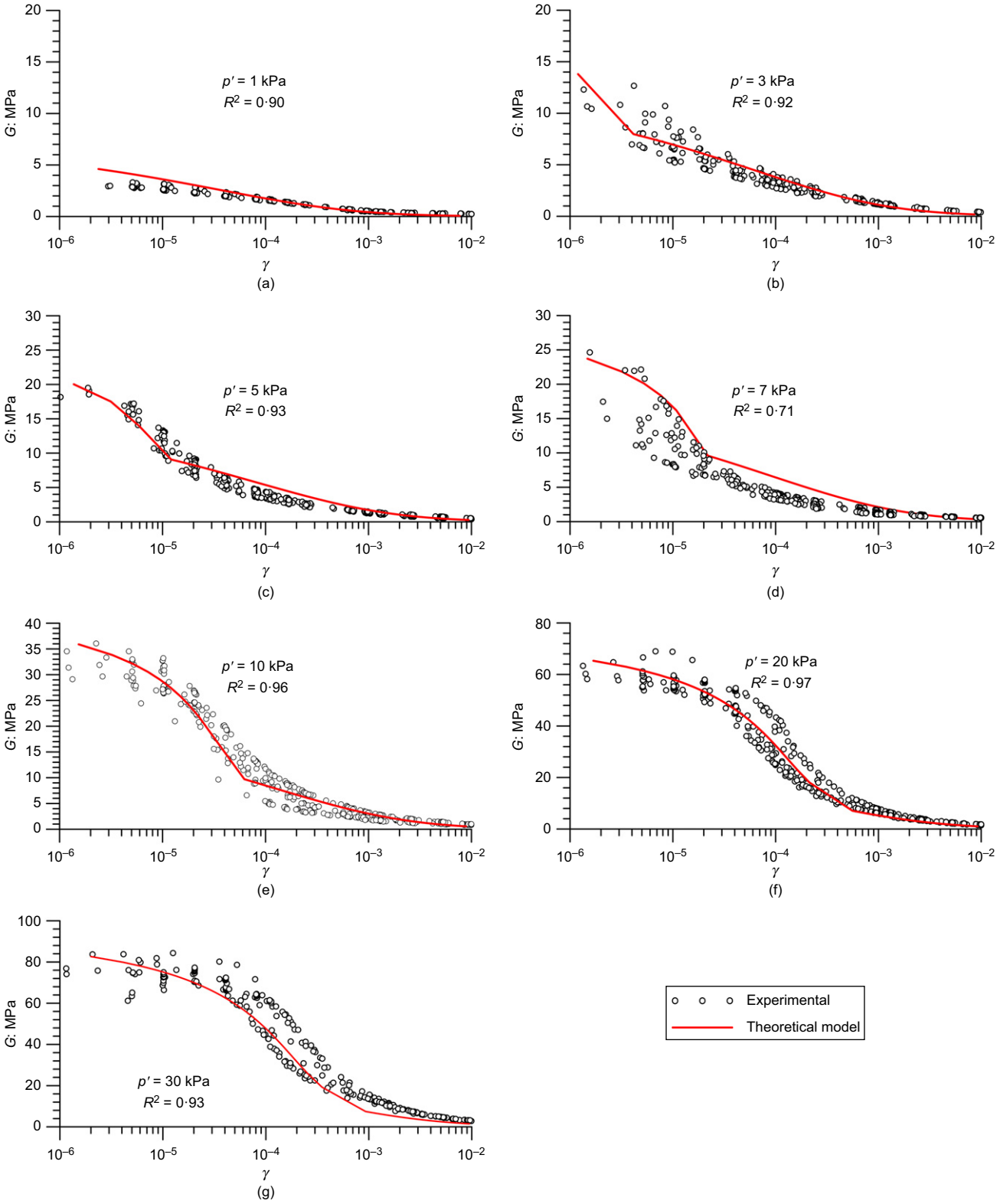

Fig. 14. Comparison between the experimental results of shear modulus (see section 'Experimental work') and the predictions of the theoretical model (see section 'Performance of the micromechanical model for the whole range of confining stresses') for the whole range of confining stresses. The parameters of the model are shown in Table 1

damping ratio at high strains, increases with the confining stress. The following equation was found after fitting the experimental results.

$$\xi^{M}(p') = 0{\cdot}2 + \frac{0{\cdot}16}{1 + e^{-0{\cdot}2(p'-15)}} \quad (p' \text{ in kPa}) \tag{34}$$

Table 1 presents the whole set of parameters of the model.

Figures 14 and 15 compare the experimental results and the data of the theoretical model for the whole range of stress presented in the earlier section 'Experimental work'. It can be observed that the agreement in shear modulus is pretty good, with a correlation coefficient higher than 0·9 (except for tests conducted under a confining pressure of 7 kPa, for which this

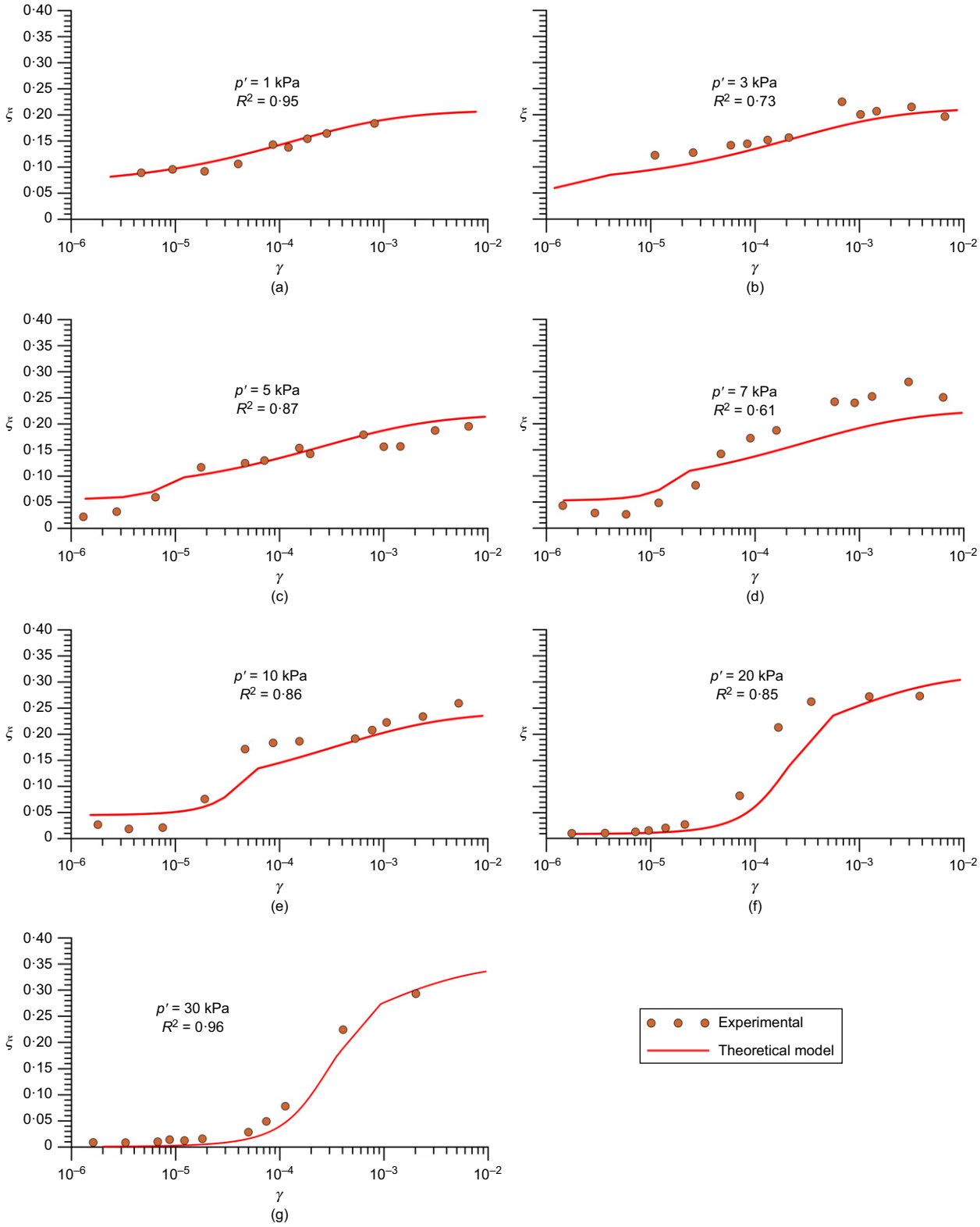

Fig. 15. Comparison between the experimental results of damping ratio (see section 'Experimental work') and the prediction of the theoretical model (see section 'Performance of the micromechanical model for the whole range of confining stresses') along the whole range of confining stresses. The theoretical model parameters are shown in Table 1

coefficient decreases to 0·71). The agreement in damping ratio, shown in Fig. 15, is reasonably good, with a correlation coefficient decreasing to 0·61 under 7 kPa, but increasing as the confining stress increases, reaching 0·96 for $p' = 30$ kPa.

In summary, the model captures, to a reasonable extent, the behaviour of dry, granular materials under low confining stresses, by accounting for both micro- and macro-mechanical characteristics. The model accurately represents the typical characteristics of soil stiffness degradation and sets a promising framework for studying soil behaviour under dynamic loading. The calibration of the model is strongly linked to the availability of a degradation curve, covering a wide range of shear strains and confining pressures; the authors are confident that extending this range of observations is beneficial to understand better the soil behaviour in uncommon conditions (e.g. extra-planetary low geostatic stresses) or overlooked scenarios (e.g. low-amplitude cyclic loading).

CONCLUSIONS

This paper presents a micromechanical model for assessing the changes in shear modulus and damping ratio in loose sands subjected to low confining stresses, a situation prevailing in particular in low-gravity conditions, in which rugosity effects at inter-grain contacts are more significant. The model is based on both the mechanical properties of the grains and the characteristics of the grains assembly, a step forward compared to models based only on fitting experimental results.

The experimental data were obtained using an innovative methodology based on a shear rheometer able to work along a broad range of shear strains (Chaparro López *et al.*, 2023). The experimental work was carried out on a loose Fontainebleau sand considered as a Martian regolith simulant at the InSight landing site.

Based on the works of Bachrach *et al.* (2000), Bahrami *et al.* (2005) and Butt *et al.* (2015), a contact theory model was developed to assess the maximum shear modulus. Then, the Hashin–Shtrikman upper bound combined two types of behaviours, one having inter-grain slippage at the microscopic level and the other one accounting for shear strength localisation. Good agreement with the experimental data was obtained for both shear modulus and damping ratio over a broader range of confining pressures.

It is important to remark that, in the current approach, modelling the changes in shear modulus requires only one fitting parameter, which depends on the confining stress. Modelling the damping ratio is, however, more empirical, with two parameters required (one constant and another one depending on the confining stress).

The model uses the volumetric portion of grains with shear-strain localisation as a fundamental parameter for describing the shear modulus degradation; in this work, such a parameter was calibrated empirically. However, it could be experimentally calibrated in future works by implementing a torsional test into an X-ray microcomputed tomography, as in Hall *et al.* (2010). Another possibility for calibrating the proportion of grains undergoing shear-strain localisation is using discrete-element computations that simulate the same shear tests, ensuring repeatability and allowing access to grain-scale quantities.

The work presented here provides a framework for studying the dynamic behaviour of loose sands submitted to low stresses. The agreement of the model is reasonably good, but it should be noted that it was applied to a uniform sand, which can reasonably be assimilated to an assembly of identical spheres. Further work is required to evaluate if this model can be applied to polydisperse granular materials with crushed grains.

ACKNOWLEDGEMENTS

The authors acknowledge Universidad de los Andes (Colombia), Ecole des Ponts ParisTech (France), together with the National Aeronautics and Space Administration (USA) NASA, the Centre National d'études spatiales (France), CNES, and their partner agencies and institutions: the United Kingdom Space Agency, UKSA, the Swiss Space Office, SSO, the Deutsches Zentrum für Luft- und Raumfahrt, DLR, the Jet Propulsion Laboratory, JPL, the Institut de Physique du Globe – Centre National de la Recherche Scientifique (France), IPGP – CNRS, the Eidgenössische Technische Hochschule *Zürich,* ETHZ, the Imperial College, London, IC, and the Max Planck institut für Sonnensystemforschung – Max Planck Gymnasium, MPS – MPG for supporting this work. This paper is InSight contribution number ICN 331.

APPENDIX. BUTT'S FITTING FUNCTION FOR THE CONTACT BETWEEN ROUGH GRAINS

The maximum displacement at the centre of the rough contact area, δ_R, given in equation (21) depends on the function $f(\gamma_R)$. Butt *et al.* (2015) propose evaluating this function through a beta function as follows:

$$f(\gamma_R) = B(0{\cdot}5, \gamma_R + 1) \tag{35}$$

The beta function $B(0{\cdot}5,\gamma_R + 1)$ is obtained based on the gamma function Γ, as follows:

$$B(0{\cdot}5, \gamma + 1) = \frac{\Gamma(1/2)\Gamma(\gamma + 1)}{\Gamma(\gamma + 1{\cdot}5)} \tag{36}$$

The following closed-form expression for the gamma function was proposed by Butt *et al.* (2015):

$$\Gamma(x+1) = a_1(x+a_2)^{x+a_2}\left(1 + \frac{a_3}{a_4 + x^{a_5}} + \frac{a_6}{x^{a_7} + a_8}\right)e^{-x^{a_9}}(2\pi)^{1/2} \tag{37}$$

The values of the constants $a_{1\ldots9}$ of function Γ were obtained by Butt *et al.* (2015) by least-squares parameter optimisation, leading to: $a_1 = 0{\cdot}5641886354$, $a_2 = 0{\cdot}500007096$, $a_3 = 0{\cdot}1091637999$, $a_4 = 1{\cdot}621840565$, $a_5 = 0{\cdot}992925298$, $a_6 = 0{\cdot}0115834573$, $a_7 = 1{\cdot}271839956$, $a_8 = 1{\cdot}505508639$, $a_9 = 1$. Note that the purpose of equation (37) is to fit function Γ in a closed form rather than in its integral form; therefore, the values $a_{1\ldots9}$ are constants, unrelated to the physics of the contact problem.

NOTATION

a	fitting parameter of the Oztoprak and Bolton equation
$a_1 \ldots a_9$	constants of the gamma function
a_H	Hertzian radius of the contact area between spherical grains
a_R	radius of the contact area between rough spherical grains
a'_R	non-dimensional contact radius
$B(0{\cdot}5,\gamma + 1)$	beta function
c	radius of the circular sticking region on particles undergoing shear forces
D_{50}	median grain size
E	Young's modulus
E'	effective Young's modulus $1/E' = (1 - \nu^2)/E$
F_N	compressive grain contact force
F_x	shear grain contact force
$f(\gamma_R)$	shape function giving the displacement between rough particles
G	shear modulus
G_0	shear modulus at low strains
G_g	shear modulus of the grains
G_{HM}	shear modulus from the Hertz–Mindlin model

G_R shear modulus of a granular arrangement of identical rough spheres
G_{RS}^{L} shear modulus for the volumetric proportion of grains undergoing localisation
$G_{RS}^{\nsim L}$ shear modulus for the volumetric proportion of grains that do not experience localisation
H_{mic} asperities microhardness
K_{HM} bulk modulus from the Hertz–Mindlin model
K_R bulk modulus of a granular arrangement of identical rough spheres
n coordination number
$P_{0,H}$ maximum stress on the contact between particles
P_0' non-dimensional pressure distribution
$p(r)$ stress on the contact area between particles
p' mean effective stress
R_g grain radius
r radius on the contact area
S_n^{HM} normal contact stiffness for perfect smooth grains
S_t^{HM} shear contact stiffness for perfect smooth grains
α_R non-dimensional parameter for characterising the grain's roughness
γ shear strain
γ_e fitting shear strain parameter of the Oztoprak & Bolton equation
γ_R stress distribution exponent
γ_r reference shear strain of the Darendeli equation
δ_H maximum displacement for a Hertz–Mindlin contact between spherical grains
δ_R maximum displacement between rough spherical grains
μ intergranular friction coefficient
μ^M macroscopic friction coefficient
ν_g Poisson's ratio of the grains
ξ damping ratio
ξ^M model parameter representing damping at large strains
ξ^μ model parameter representing damping at low strains
σ_{rms} root mean square asperities height
τ_0 shear stress at the middle of the contact area
τ_{mob} normalised mobilised shear strength
τ_{mob}^M macroscopic normalised shear strength mobilisation
τ_{mob}^μ inter-grain shear strength mobilisation
$\tau(r)$ shear stress on a point located at a radius r of the contact area
τ_R non-dimensional parameter for characterising the grain's roughness
ϕ porosity
ψ volumetric proportion of grains that do not experience localisation

REFERENCES

Altuhafi, F. N., Coop, M. R. & Georgiannou, V. N. (2016). Effect of particle shape on the mechanical behavior of natural sands. *J. Geotech. Geoenviron. Engng* **142**, No. 12, 04016071.

Andria-Ntoanina, I. (2011). *Caractérisation dynamique de sables de référence en laboratoire- application à la réponse sismique de massifs sableux en centrifugeuse*. PhD thesis, Ecole des Ponts ParisTech, Champs-sur-Marne, France.

Archard, J. F. (1957). Elastic deformation and the laws of friction. *Proc. R. Soc. A: Math. Phys. Engng* **243**, No. 1233, 190–205.

Bachrach, R., Dvorkin, J. & Nur, A. M. (2000). Seismic velocities and Poisson's ratio of shallow unconsolidated sands. *Geophysics* **65**, No. 2, 559–564.

Bahrami, M., Yovanovich, M. M. & Culham, J. R. (2005). A compact model for spherical rough contacts. *J. Tribol. Oct.* **127**, No. 4, 884–889, https://doi.org/10.1115/1.2000982.

Butt, S. U., Antoine, J. F. & Martin, P. (2015). Simplified stiffness model for spherical rough contacts. *Tribol. – Mater. Surf. Interfaces* **9**, No. 2, 63–70.

Caicedo, B. (2018). *Geotechnics of roads: fundamentals*. Boca Raton, FL, USA: CRC Press.

Caicedo, B., Castillo Betancourt, J. P., Delage, P., Lognonné, P. & Banerdt, B. (2023). Wave velocities and Poisson ratio in a loose sandy Martian regolith simulant under low stresses: 2. Theoretical analysis. *J. Geophys. Res. Planets* **128**, No. 11, https://doi.org/10.1029/2023JE008008.

Caro, S., Sánchez, D. B. & Caicedo, B. (2015). Methodology to characterise non-standard asphalt materials using DMA testing: application to natural asphalt mixtures. *Int. J. Pavement Engng* **16**, No. 1, 1–10.

Castillo Betancourt, J. P., Delage, P., Caicedo, B., Lognonné, P. & Banerdt, B. (2023). Wave velocities and Poisson ratio in a loose sandy Martian regolith simulant under low stresses: 1. Laboratory investigation. *J. Geophys. Res. Planets* **128**, No. 11, e2023JE007988, https://doi.org/10.1029/2023JE007988.

Chaparro López, M. J., Castillo-Betancourt, J. P., Cabrera, M., Caicedo, B., Delage, P., Lognonné, P. & Banerdt, B. (2023). Dynamic mechanical analysis test for evaluating loose sands on a wide strain range–application to the InSight mission on mars. *Geotech. Test. J.* **46**, No. 6, https://doi.org/10.1520/GTJ20230381.

Darendeli, B. M. (2001). *Development of a new family of normalized modulus reduction and material damping curves*. PhD dissertation, University of Texas, Austin, TX, USA.

Delage, P., Karakostas, F., Dhemaied, A., Belmokhtar, M., Lognonné, P., Golombek, M., de Laure, E., Hurst, K., Dupla, J. C., Kedar, S., Cui, Y. J. & Banerdt, B. (2017). An investigation of the mechanical properties of some Martian regolith simulants with respect to the surface properties at the InSight mission landing site. *Space Sci. Rev.* **211**, No. 1–4, 191–213, https://doi.org/10.1007/s11214-017-0339-7.

Delage, P., Betancourt, J. P. C., Caicedo Hormaza, B., Karakostas, F., De Laure, E., Lognonné, P., Antonangeli, D. & Banerdt, B. (2022a). The interaction between the SEIS seismometer of the InSight Martian mission and a regolith simulant. *Géotechnique* **74**, No. 1, 42–53, https://doi.org/10.1680/jgeot.21.00171.

Delage, P., Marteau, E., Vrettos, C., Golombek, M. P., Ansan, V., Banerdt, W. B., Grott, M., Hurst, K., Lognonné, P., Murdoch, N., Piqueux, S., Schmelbach, C., Spohn, T., Warner, N., Widmer-Schnidrig, R., Brinkman, N., Caicedo-Hormaza, B., Castillo-Betancourt, J. P., Edme, P., Kedar, S., Lange, L., Lemmon, M., Mueller, N., Onodera, K., Robertsson, J., Sollberger, D., Stähler, S., Verdier, N. & Williams, N. R. (2022b). The mechanical properties of the Martian soil at the InSight landing site. In *Proceedings 20th international conference on soil mechanics and geotechnical engineering*. Sydney, Australia: ISSMGE.

Digby, P. J. (1981). The effective elastic moduli of porous granular rocks. *J. Appl. Mech.* **48**, No. 4, 803–808.

Duffaut, K., Landrø, M. & Sollie, R. (2010). Using Mindlin theory to model friction-dependent shear modulus in granular media. *Geophysics* **75**, No. 3, E143–E152.

Golombek, M. P., Haldemann, A. F. C., Simpson, R. A., Fergason, R. L., Putzig, N. E., Arvidson, R. E., Bell, J. F. & Mellon, M. T. (2009). Martian surface properties from joint analysis of orbital, earth-based, and surface observations. In *The Martian surface: Composition, mineralogy and physical properties*, (ed. J. Bell), pp. 468–498, https://doi.org/10.1017/cbo9780511536076.022. Cambridge, UK: Cambridge University Press.

Golombek, M., Kipp, D., Warner, N., Daubar, I. J., Fergason, R., Kirk, R. L., Beyer, R., Huertas, A., Piqueux, S., Putzig, N. E., Campbell, B. A., Morgan, G. A., Charalambous, C., Pike, W. T., Gwinner, K., Calef, F., Kass, D., Mischna, M., Ashley, J., Bloom, C., Wigton, N., Hare, T., Schwartz, C., Gengl, H., Redmond, L., Trautman, M., Sweeney, J., Grima, C., Smith, I. B., Sklyanskiy, E., Lisano, M., Benardini, J., Smrekar, S., Lognonné, P. & Banerdt, W. B. (2017). Selection of the InSight landing site. *Space Sci. Rev.* **211**, 5–95.

Golombek, M., Warner, N. H., Grant, J. A., Hauber, E., Ansan, V., Weitz, C. M., Williams, N., Charalambous, C., Wilson, S. A., DeMott, A., Kopp, M., Lethcoe-Wilson, H., Berger, L., Hausmann, R., Marteau, E., Vrettos, C., Trussell, A., Folkner, W., le Maistre, S., Mueller, N., Grott, M., Spohn, T., Piqueux, S., Millour, E., Forget, F., Daubar, I., Murdoch, N., Lognonné, P., Perrin, C., Rodriguez, S., Pike, W. T., Parker, T., Maki, J., Abarca, H., Deen, R., Hall, J., Andres, P., Ruoff, N., Calef, F., Smrekar, S., Baker, M. M., Banks, M., Spiga, A., Banfield, D., Garvin, J., Newman, C. E. & Banerdt, W. B.

(2020). Geology of the InSight landing site on Mars. *Nat. Communs* **11**, No. 1, 1–11, https://doi.org/10.1038/s41467-020-14679-1.

Greenwood, J. A. & Tripp, J. H. (1967). The elastic contact of rough spheres. *ASME J. Appl. Mech.* **34**, No. 1, 153–159, https://doi.org/10.1115/1.3607616.

Greenwood, J. A. & Williamson, B. P. (1966). Contact of nominally flat surfaces. *Proc. Phys. Soc., Lond., Sect. A* **295**, No. 1442, 300–319.

Hall, S. A., Bornert, M., Desrues, J., Pannier, Y., Lenoir, N., Viggiani, G. & Bésuelle, P. (2010). Discrete and continuum analysis of localised deformation in sand using X-ray μCT and volumetric digital image correlation. *Géotechnique* **60**, No. 5, 315–322, https://doi.org/10.1680/geot.2010.60.5.315.

Hardin, B. O. & Drnevich, V. P. (1972a). Shear modulus and damping in soils: measurement and parameter effects. *J. Soil Mech. Found. Div.* **98**, No. SM6, 603–624.

Hardin, B. O. & Drnevich, V. P. (1972b). Shear modulus and damping in soils: design equations and curves. *J. Geotech. Engng* **98**, No. 7, 667–692.

Hashin, S. & Shtrikman, S. (1963). A variational approach to the elastic behavior of multiphase materials. *J. Mech. Phys. Solids* **11**, No. 2, 127–140.

Hertz, H. (1882). Über dieBeruhrüng fester elastischer Körper. *J. für die Reine und Angew. Math.* **92**, 156–171 (in German).

Hughes, J. & Whittle, R. (2022). *High resolution pressuremeters and geotechnical engineering: the measurement of small things*. Boca Raton, FL, USA: CRC Press.

Kramer, S. L. (1996). *Geotechnical earthquake engineering*. Pearson Education India.

Lognonné, P., Banerdt, W. B., Giardini, D., Pike, W. T., Christensen, U., Laudet, P. & Berenguer, J. L. (2019). SEIS: Insight's seismic experiment for internal structure of Mars. *Space Sci. Rev.* **215**, No. 1, 1–170.

Lognonné, P., Banerdt, W. B., Pike, W. T., Giardini, D., Christensen, U., Garcia, R. F., Kawamura, T., Kedar, S., Knapmeyer-Endrun, B., Margerin, L., Nimmo, F., Panning, M., Tauzin, B., Scholz, J.-R., Antonangeli, D., Barkaoui, S., Beucler, E., Bissig, F., Brinkman, N., Calvet, M., Ceylan, S., Charalambous, C., Davis, P., van Driel, M., Drilleau, M., Fayon, L., Joshi, R., Kenda, B., Khan, A., Knapmeyer, M., Lekic, V., McClean, J., Mimoun, D., Murdoch, N., Pan, L., Perrin, C., Pinot, B., Pou, L., Menina, S., Rodriguez, S., Schmelzbach, C., Schmerr, N., Sollberger, D., Spiga, A., Stähler, S., Stott, A., Stutzmann, E., Tharimena, S., Widmer-Schnidrig, R., Andersson, F., Ansan, V., Beghein, C., Böse, M., Bozdag, E., Clinton, J., Daubar, I., Delage, P., Fuji, N., Golombek, M., Grott, M., Horleston, A., Hurst, K., Irving, J., Jacob, A., Knollenberg, J., Krasner, S., Krause, C., Lorenz, R., Michaut, C., Myhill, R., Nissen-Meyer, T., ten Pierick, J., Plesa, A.-C., Quantin-Nataf, C., Robertsson, J., Rochas, L., Schimmel, M., Smrekar, S., Spohn, T., Teanby, N., Tromp, J., Vallade, J., Verdier, N., Vrettos, C., Weber, R., Banfield, D., Barrett, E., Bierwirth, M., Calcutt, S., Compaire, N., Johnson, C. L., Mance, D., Euchner, F., Kerjean, L., Mainsant, G., Mocquet, A., Rodriguez Manfredi, J. A., Pont, G., Laudet, P., Nebut, T., de Raucourt, S., Robert, O., Russell, C. T., Sylvestre-Baron, A., Tillier, S., Warren, T., Wieczorek, M., Yana, C. & Zweifel, P. (2020). Constraints on the shallow elastic and anelastic structure of Mars from InSight seismic data. *Nat. Geosci.* **13**, 213–220, https://doi.org/10.1038/s41561-020-0536-y.

Majumdar, A. & Bhushan, B. (1991). Fractal model of elastic-plastic contact between rough surfaces. *ASME J. Tribol.* **113**, No. 1, 1–11.

Mavko, G., Mukerji, T. & Dvorkin, J. (1998). *The rock physics handbook*. Cambridge, UK: Cambridge University Press.

Mindlin, R. D. (1949). Compliance of elastic bodies in contact. *J. Appl. Mech.* **16**, No. 3, 259–268.

Morgan, P., Grott, M., Knapmeyer-Endrun, B., Golombek, M., Delage, P., Lognonné, P. & … Kedar, S. (2018). A pre-landing assessment of regolith properties at the InSight landing site. *Space Sci. Rev.* **214**, No. 6, 1–47.

Mueller, N., Piqueux, S., Lemmon, M., Maki, J., Lorenz, R. D., Grott, M., Spohn, T., Smrekar, S. E., Knollenberg, J., Hudson, T. L., Krause, C., Millour, E., Forget, F., Golombek, M., Hagermann, A., Attree, N., Siegler, M. & Banerdt, W. B. (2021). Near surface properties of Martian regolith derived from InSight HP3-RAD temperature observations during phobos transits. *Geophys. Res. Lett.* **48**, No. 15, e2021GL093542.

Nardelli, V. & Coop, M. R. (2019). The experimental contact behaviour of natural sands: normal and tangential loading. *Géotechnique* **69**, No. 8, 672–686, https://doi.org/10.1680/jgeot.17.P.167.

Otsubo, M., O'sullivan, C., Sim, W. W. & Ibraim, E. (2015). Quantitative assessment of the influence of surface roughness on soil stiffness. *Géotechnique* **65**, No. 8, 694–700, https://doi.org/10.1680/geot.14.T.028.

Oztoprak, S. & Bolton, M. D. (2013). Stiffness of sands through a laboratory test database. *Géotechnique* **63**, No. 1, 54–70, https://doi.org/10.1680/geot.10.P.078.

Persson, B. N. (2006). Contact mechanics for randomly rough surfaces. *Surf. Sci. Rep.* **61**, No. 4, 201–227.

Poblete, M., Wichtmann, T., Niemunis, A. & Triantafyllidis, T. (2015). Caracterización cíclica multidimensional de suelos no cohesivos. *Obras y Proyectos* **17**, 31–37.

Popov, V. (2010). *Contact mechanics and friction: physical principles and applications*. Berlin, Germany: Springer.

Radjai, F., Jean, M., Moreau, J. J. & Roux, S. (1996). Force distributions in dense two-dimensional granular systems. *Phys. Rev. Lett.* **77**, No. 2, 274.

Reddy, N. S., He, H. & Senetakis, K. (2022). DEM Analysis of small and small-to-medium strain shear modulus of sands. *Comput. Geotech.* **141**, 104518, https://doi.org/10.1016/j.compgeo.2021.104518.

Seed, H. B. & Idriss, I. M. (1970). *Soil moduli and damping factors for dynamic response analyses*, Report EERC 70-10. Berkeley, CA, USA: University of California.

Senetakis, K., Coop, M. R. & Todisco, M. C. (2013a). Tangential load–deflection behaviour at the contacts of soil particles. *Géotechnique Lett.* **3**, No. 2, 59–66, https://doi.org/10.1680/geolett.13.00019.

Senetakis, K., Coop, M. R. & Todisco, M. C. (2013b). The inter-grain coefficient of friction at the contacts of Leighton Buzzard sand quartz minerals. *Soils Found.* **53**, No. 5, 746–755.

TA Instruments (2007). AR 2000 rheometer rheometrics series operator's manual.

Villacreses, J. P., Caicedo, B., Caro, S. & Yépez, F. (2020). A novel procedure to determine shear dynamic modulus and damping ratio for partial saturated compacted fine-grained soils. *Soil Dyn. Earthq. Engng* **131**, 106029, https://doi.org/10.1016/j.soildyn.2019.106029.

Walton, K. (1987). The effective elastic moduli of a random packing of spheres. *J. Mech. Phys. Solids* **35**, No. 2, 213–226.

Yimsiri, S. & Soga, K. (2000). Micromechanics-based stress–strain behaviour of soils at small strains. *Géotechnique* **50**, No. 5, 559–571, https://doi.org/10.1680/geot.2000.50.5.559.

Yimsiri, S. & Soga, K. (2011). Effects of soil fabric on behaviors of granular soils: microscopic modeling. *Comput. Geotech.* **38**, No. 7, 861–874.

Yovanovich, M. (2006). Micro and macro hardness measurements, correlations, and contact models. In 44th AIAA aerospace sciences meeting and exhibit, Reno, NV, USA, AIAA 2006-979, https://doi.org/10.2514/6.2006-979.